PAPER

Check for updates

Cite this: *RSC Adv.*, 2019, **9**, 4469

Dielectric and photoluminescence properties of fine-grained BaTiO₃ ceramics co-doped with amphoteric Sm and valence-variable Cr

Dandan Han, [iD] [ab] Dayong Lu*[b] and Fanling Meng*[a]

$(Ba_{1-x}Sm_x)(Ti_{1-x}Cr_x)O_3$ (BSTC) and $(Ba_{1-x}Sm_x)(Ti_{1-(x-0.01)}Cr_{x-0.01})O_3$ (BSTC1) ceramics with a single-phase perovskite structure were prepared using a traditional solid state based method. The structure, microstructure, site occupations, valence states of Cr, photoluminescence, and dielectric properties of these ceramics were investigated using XRD, SEM, EDXS, RS, EPR, XPS, and dielectric measurements. All ceramics exhibit a fine-grained microstructure (0.7 μm). Three valence states of Cr ions were confirmed and Cr predominates as Cr^{3+} enter the Ti^{4+} sites with a stronger EPR signal (1.974). The RS bands of high-wavenumber were attributed to photoluminescence from Sm^{3+} ions. The formation of $Sm^{\bullet}_{Ba} - Cr'_{Ti}$ defect complexes play leading roles in the removal of $V^{\bullet\bullet}_O$, prevent the grain growth, and photoluminescence quenching. $(Ba_{1-x}Sm_x)(Ti_{1-(x-0.01)}Cr_{x-0.01})O_3$ (BSTC1) ceramics with amphoteric Sm^{3+} ions exhibit a regular diffuse phase transition behavior, rapid T_m-shifting rate of -24.3 °C/at% (Sm/Cr), higher ε'_{RT}, lower tan δ and x = 0.04 and 0.05 met the EIA Y5V specification.

1. Introduction

Barium titanate (BaTiO₃) ceramics represent a materials system of fundamental importance for a wide range of technical applications in the field of ceramic capacitors, ferroelectric sensors, optoelectronic devices, actuators, and so on.[1–4] During the past few decades, 3d transition metal elements with variable valence as effective acceptor dopants of BaTiO₃ ceramics have been mainly applied in ceramic capacitors.[4–8] The hexagonal phase can be stabilized at room temperature by doping 3d transition metal acceptors[4,5] and may be attributed to Jahn–Teller distortion (such as Cr_{Ti}^{4+} (d²) or Cr_{Ti}^{5+} (d¹)). In addition, most of these reported BaTiO₃-based ceramics using doping 3d transition metal elements have one significant drawback: during sintering at high temperature oxygen vacancies ($V^{\bullet\bullet}_O$) and conduction electrons are easily created,[6] leading to leakage conductance and making the dielectric material into a semiconductor.

The smaller rare-earth ions (*e.g.* La (1.36 Å), Nd (1.27 Å) and Sm (1.24 Å)) compared with Ba^{2+} (1.61 Å) were found to be effective in improving dielectric permittivity and suppressing the hexagonal phase, and forming a single-phase BaTiO₃-based ceramic. When rare-earth ions or metal ions

are simultaneous substitution on Ba^{2+} sites and Ti^{4+} sites, such as $(Ba_{1-x}Nd_x)(Ti_{1-x}Mn_x)O_3$,[5] $(Ba_{1-x}La_x)(Ti_{1-x}Cr_x)O_3$,[7] $(Ba_{1-x}Nd_x)(Ti_{1-x}Fe_x)O_3$,[8] $(Ba_{1-x}Na_x)(Ti_{1-x}Nb_x)O_3$,[9,10] $(Ba_{1-x}Sr_x)(Ti_{1-y}Zr_y)O_3$,[11] $(Ba_{1-x}La_x)(Ti_{1-x}Yb_x)O_3$,[12] $(Ba_{1-x}Gd_x)(Ti_{1-x}Sc_x)O_3$,[13] $Ba_{1-x}Ln_xTi_{1-x}M_xO_3$ (Ln = La, Sm, Gd, Dy. M = Al, Fe, Cr),[14] then it is expected that the charge compensation is maintained internally without requiring the creation of defects. These double substitutions BaTiO₃-based composites have many advantages over the single substitution in inhibiting grain growth, superior long-term reliability, and high-*k* Y5V dielectric behavior (note: Electronic Industries Alliance (EIA) code, Y5V specification: $-82\% \leq (\varepsilon' - \varepsilon'_{RT})/\varepsilon'_{RT} \leq +22\%$ in a temperature range of -30 to 85 °C).

In this work, $(Ba_{1-x}Sm_x)(Ti_{1-x}Cr_x)O_3$ (BSTC) and $(Ba_{1-x}Sm_x)(Ti_{1-(x-0.01)}Cr_{x-0.01})O_3$ (BSTC1) ceramics were prepared using a traditional solid state based method. Sm and Cr are used as co-dopants in BaTiO₃ based on the following: (1) Sm ions acting as a donor, predominantly dissolves in Ba^{2+} sites and induces a common feature of high-*k* first phase transition (FPT) behavior;[14–22] Sm is also known to be an amphoteric dopant in Ba^{2+} sites and Ti^{4+} sites for BaTiO₃, similar to (Ce[23] and Dy[24]) substitution. It would be interesting to investigate the site occupation of Sm ions; and (2) to investigate the photoluminescence properties of Sm ions. It is well known as good red activators in many matrices due to the $^4G_{5/2} \rightarrow {}^6H_{I/2}$ ($I = 5$, 7, 9) transitions of Sm^{3+} in Ba^{2+} sites;[18–22] and (3) Cr^{3+} in Ti^{4+} sites acted as a charge compensator and the main valence state of Cr substituted on Ti^{4+} sites is changeable. Cr is a element with multiple valence states from +2 to +6. Cr in BaTiO₃ is

[a]Key Laboratory of Automobile Materials, Ministry of Education, College of Materials Science and Engineering, Jilin University, Changchun 130012, China. E-mail: mfl@jlu.edu.cn

[b]Research Center for Materials Science and Engineering, Jilin Institute of Chemical Technology, Jilin 132022, P. R. China. E-mail: dylu@jlict.edu.cn; Tel: +86 0432 62815308

known to be substituted on the Ti^{4+} sites[25–27] due to its closer ionic size {Cr^{3+} ($3d^3$) (0.615 Å), Cr^{4+} ($3d^2$) (0.55 Å), Cr^{5+} ($3d^1$) (0.49 Å)} to Ti^{4+} (0.605 Å).[28] Langhammer reported[29] that in air-sintered ceramics chromium is incorporated with valence states 3+ and 4+ when Cr_2O_3 is chosen as dopant. Moreover, Cr^{6+} are reduced into Cr^{4+} and Cr^{5+} for oxidized sample when Cr^{6+} ions doped in $BaTiO_3$. Qi indicated that when the acceptor-doped samples were prepared under air condition, due to enough oxygen existence and on the basis of charge balance, the Cr^{3+} ($3d^3$) can be partly oxidized to form Cr^{5+} ($3d^1$).[30] Our results confirmed that mixed valence states of $Cr^{3+}/Cr^{5+}/Cr^{6+}$ existed in BSTC and BSTC1. In addition, one encouraging note is that the reduction in Cr concentration by 1% for BSTC1 compared to BSTC induced a regular diffuse phase transition (DPT) behavior. The related works for $BaTiO_3$ ceramics co-doped with amphoteric Sm and valence-variable Cr been rarely reported to date.

2. Experimental

2.1. Synthesis

Ceramics raw materials were reagent-grade $BaCO_3$ (Sinopharm Chemical Reagent, 99.4%), TiO_2 (Shanghai Yuejiang Powders, anatase, 99.5%), Sm_2O_3 (Shanghai Diyang Chemical, 99.99%) and Cr_2O_3 (Sinopharm Chemical Reagent, 99.0%) powders. The ceramics $(Ba_{1-x}Sm_x)(Ti_{1-x}Cr_x)O_3$ ($x = 0.01, 0.02, 0.03, 0.04, 0.05$) (abbreviated BSTC) and $(Ba_{1-x}Sm_x)(Ti_{1-(x-0.01)}Cr_{x-0.01})O_3$ ($x = 0.02, 0.03, 0.04, 0.05$) (BSTC1) were prepared according to the nominal compositions using a traditional solid state based method.[8] $(Ba_{1-x}Sm_x)Ti_{1-x/4}O_3$ ($x = 0.05$) (abbreviated S5), $Ba(Ti_{1-x}Cr_x)O_3$ ($x = 0.05$) (abbreviated Cr5) and pure $BaTiO_3$ ceramics were prepared under the same conditions as BSTC and BSTC1 for comparison. Accurately weighed raw material powders (weighing accuracy reaches 0.0002) were carefully dry-mixed and ground in an agate mortar and then calcined at 1100 °C for 5 h in air at a heating rate of 350 °C h^{-1}. The calcined powders were mixed thoroughly with an aqueous PVA solution (12% by mass) and pressed uniaxially at 200 MPa into disk-like pellets (six pellets of each composition) with 12 mm diameters and 2.0 mm thickness. The final sintering conditions to form the ceramics were chosen as 1400 °C for 12 h in air at a heating rate of 100 °C h^{-1}, a cooling rate of −200 °C h^{-1} to 700 °C and then furnace-cooled to room temperature.

2.2. Characterization

Structural characterization of ceramics was performed by powder X-ray diffraction (XRD) using a DX-2700 X-ray diffractometer (Dandong Haoyuan). Lattice parameters were calculated by MS Modeling (Accelrys) using the Reflex Package and Cu Kα_1 radiation ($\lambda = 1.540562$ Å).

The microstructure was observed using an EVOMA 10 scanning electric microscope (SEM, Zeiss) operated at 15 kV. All ceramics were polished by coarse grinding using diamond grinding plate and fine grinding using diamond paste (grain size: 0.25 mm). The thermal etching at 1400 °C for 12 min was then performed with a heating rate of 6 °Cmin^{-1} and natural cooling. Finally, the conducting Au atoms were sputtered on the specimen surface for SEM observations. To observe the potential secondary phases, SEM investigations in BSE (backscattered electron) mode were performed. An Aztec 2.3 energy-dispersive X-ray spectrometer (EDXS) (Oxford Instruments) was attached to the SEM for compositional analyses.

The 532 and 638 nm laser was used for excitation in obtaining the Raman spectra (RS) of the ceramics and photoluminescence (PL) of Sm^{3+} using a LabRAM XploRA Raman spectrometer (Horiba Jobin Yvon).

Electron paramagnetic resonance (EPR) spectra were measured at room temperature using an A300 electron-spin resonance spectrometer system (Bruker BioSpin GMBH, Germany) at an X-band frequency of 9.86 GHz. The EPR cavity of the spectrometer was changed with an ER 4102ST cavity for temperature-dependent EPR measurements at −183 °C with an X-band frequency of 9.44 GHz. The gyromagnetic factor (g) was calculated by the relationship $h\nu_0 = g\beta H$, where h is the Planck constant ($h = 6.626 \times 10^{-34}$ J s), ν_0 is the microwave frequency, β is the Bohr magnetron ($\beta = 9.262 \times 10^{-24}$ J T^{-1}), H is the magnetic field strength.

X-ray photoelectron spectra (XPS) measurements were performed at room temperature using an ESCALAB 250 X-ray photoelectron spectrometer (Thermo Electron). The XPS data raw were processed by smoothing multiply times and the background type of shirley was used for XPS fitting.

The temperature dependences of the dielectric permittivity and the dielectric loss were measured at 1 kHz from −75 to 200 °C at a heating rate of 2 °C min^{-1} using a Concept 41 Dielectric/Impedance Spectrometer (Novocontrol) with an applied voltage of 1 V (AC). To meet test conditions and give nice pellet surfaces, these ceramics were polished to 0.8 mm thickness by coarse grinding and fine grinding using 1200# and 2000# diamond grinding plate, respectively. The drying was then performed at 500 °C for 120 min and natural cooling. Finally, the surfaces of the polished ceramic disks were sputtered with thin Au atoms and silver paste (5 mm × 5 mm) to form the contact electrodes for the dielectric measurements.

3. Results and discussion

3.1. X-ray diffraction analysis

Powder XRD patterns for BSTC and BSTC1 ceramics are shown in Fig. 1. BSTC and BSTC1 exhibit single-phase perovskite structures. No impurity phases are observed within the XRD instrument limits. Tetragonal for $x \leq 0.03$, characteristic of two separate (002) and (200) peaks, and cubic for $x \geq 0.04$ marked by a symmetric (200) peak, $i.e.$ that the tetragonal-cubic phase transition occurred at $x = 0.04$ in these two series of ceramics (Fig. 1(b) and (d)).

Fig. 2(a) shows the variations in unit-cell volume (V_0) as a function of x for BSTC and BSTC1. Two insets depict the tetragonality (c/a) $versus$ x, and it shows that c/a decreases approximately linearly and $c/a = 1$ (cubic phase) at $x = 0.04$. The V_0 of BSTC and BSTC1 are less than that of the tetragonal $BaTiO_3$ (64.41 Å^3, from JCPDS cards no. 05-626) and it decreases with x, approximately following Vegard's law. The V_0–x curve of BSTC is lower than that of BSTC1. Meanwhile, when Sm
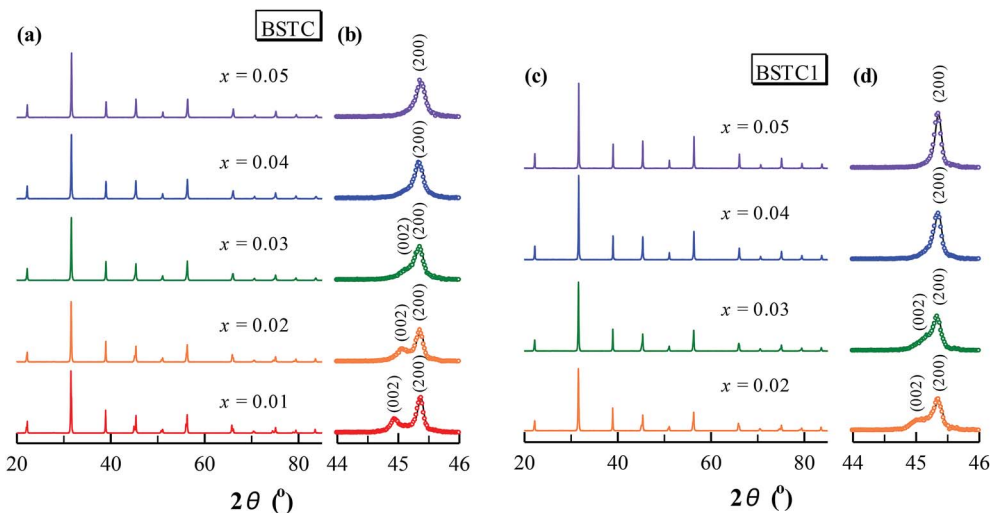
Fig. 1 Powder XRD patterns of (a) $(Ba_{1-x}Sm_x)(Ti_{1-x}Cr_x)O_3$ ($x = 0.01-0.05$) (BSTC) and (c) $(Ba_{1-x}Sm_x)(Ti_{1-(x-0.01)}Cr_{x-0.01})O_3$ ($x = 0.02-0.05$) ceramics (BSTC1); XRD peaks in the vicinity of 45° for (b) BSTC and (d) BSTC1.
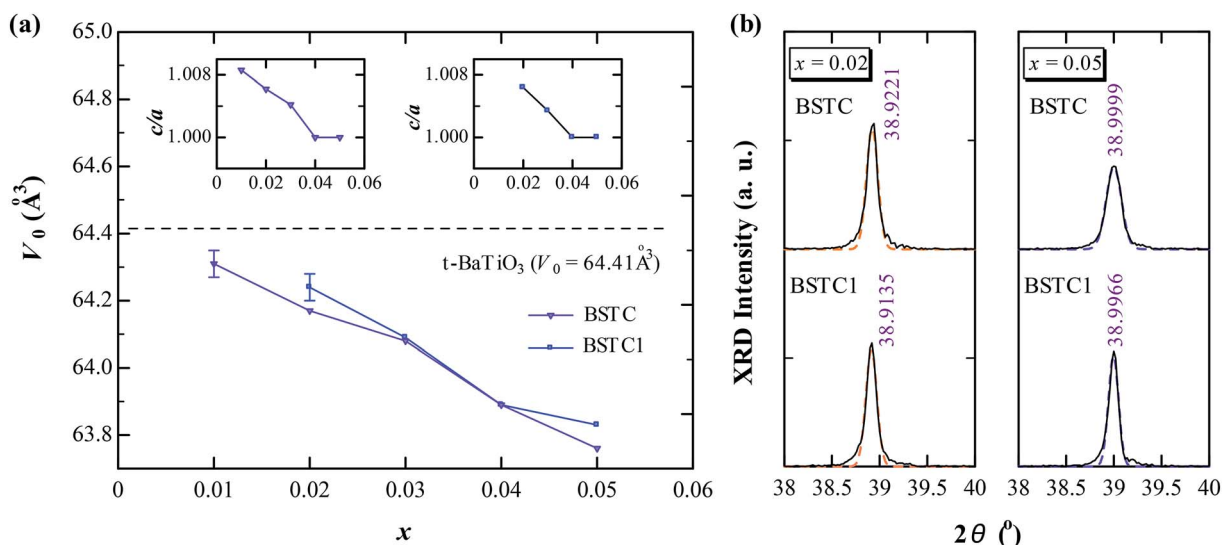

Fig. 2 (a) Variations in unit cell volume (V_0) as a function of x for BSTC and BSTC1; (b) XRD (111) peak profiles for BSTC and BSTC1 with 0.02 and 0.05. The dashed lines are Gaussian fitting of the peaks.

concentration is equal for BSTC and BSTC1 ($x = 0.02$ and 0.05), the (111) diffraction peak in the vicinity of 39° (Fig. 2(b)) shifts towards a higher angle with the increase of Cr concentration, which suggests that there is a lattice contraction. The result is an abnormal phenomenon because Cr^{3+} ($3d^3$) (0.615 Å) ion is greater than Ti^{4+} ion.

So, on the basis of a simple ionic size comparison, the XRD results draw two conclusions: (1) Sm ions (1.24 Å) predominant occupied the Ba^{2+} sites; and (2) the intermediate ionic size rare-earth ions Sm inevitably occupy the other site no matter which site is designed especially that the reduction in Cr concentration by 1% compared to Sm for BSTC1 ceramics, and Sm^{3+} (0.958 Å) doping at Ti^{4+} sites has a larger ionic radius, which is the direct reason for the contraction in V_0 for BSTC with $x = 0.02$ and 0.05 relative to BSTC1 (Fig. 2(b)).

3.2. Microstructure

SEM images of these ceramics are shown in Fig. 3. Because of the amounts of these impurity phases may be too small to be detected by XRD, BSE image of BSTC with $x = 0.05$ was also performed to detect these potential impurity phases (Fig. 3). No abnormal region was observed. The result indicated that no core–shell grains and impurity phases were observed for BSTC and BSTC1 ceramics. All sintered ceramic samples except BSTC with $x = 0.01$ (a bimodal microstructure consisting of coarse grains (>2.5 μm) and fine grains (~1.0 μm)) were found to exhibit a uniform grain size (~0.7 μm), independent of x, especially the specimen BSTC1 with $x = 0.05$ exhibited homogeneous and dense-grained microstructure. The SEM data indicated Sm and Cr had an effect on the primary particle size.
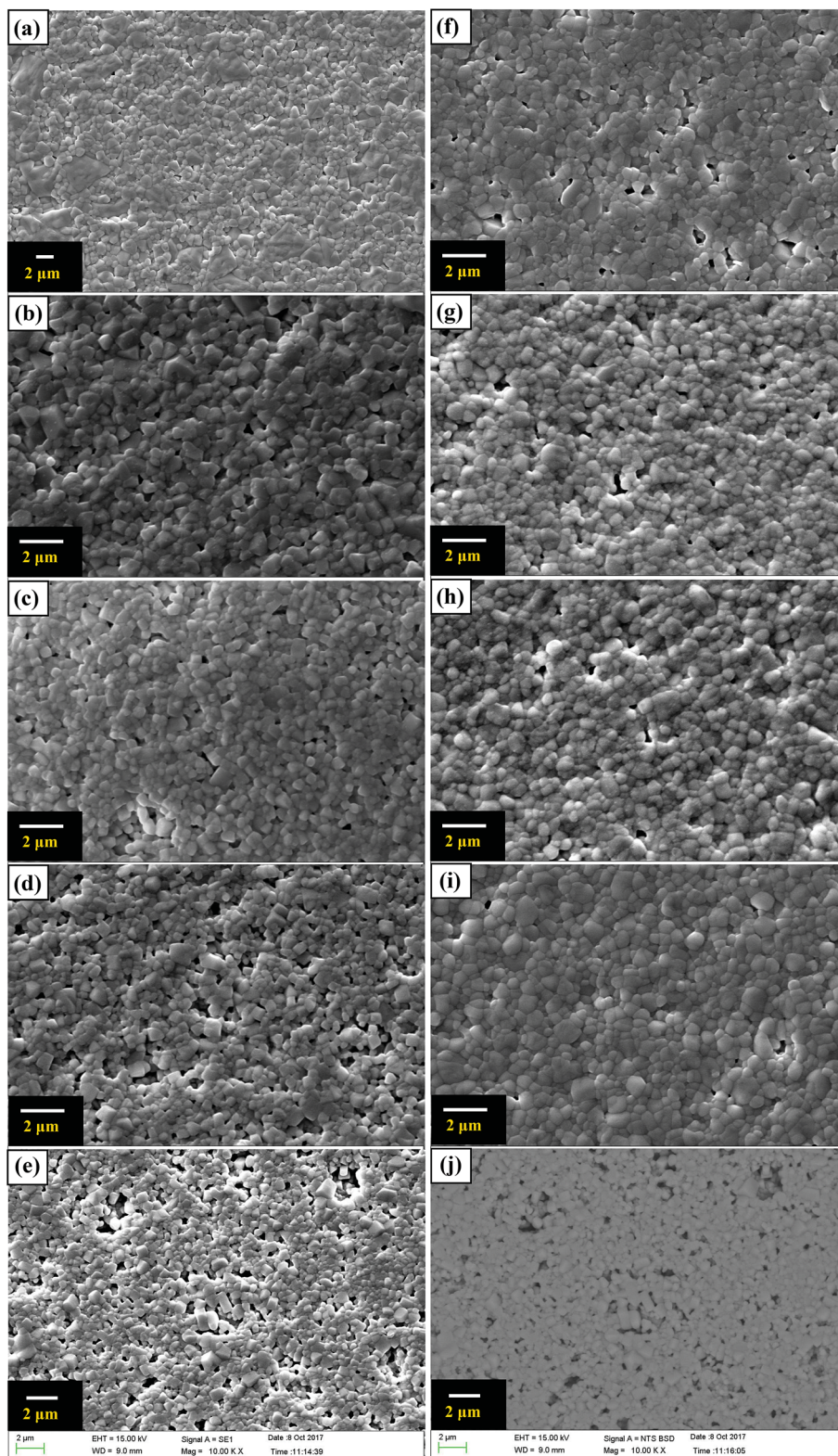
Fig. 3 SEM image of BSTC ceramics with $x =$ (a) 0.01, (b) 0.02, (c) 0.03, (d) 0.04, (e) 0.05, and BSTC1 ceramics with $x =$ (f) 0.02, (g) 0.03, (h) 0.04, (i) 0.05. BSE images analyses of BSTC ceramics with $x =$ (j) 0.05.

This can be explained that lattice distortion caused by the generation of $Sm^{\bullet}_{Ba} - Cr'_{Ti}$ defect complexes will consume some energy, this hindered the grain boundary migration and prevented the grain growth.[3,31,32]

Some blue deposits on the bottom of Al_2O_3 crucible in the process of sintering could be because Cr^{6+} can combine O^{2-} to constitute the CrO_3, which volatilizes at high temperature condition.[30,33] The EDXS of BSTC and BSTC1 with $x = 0.05$ are
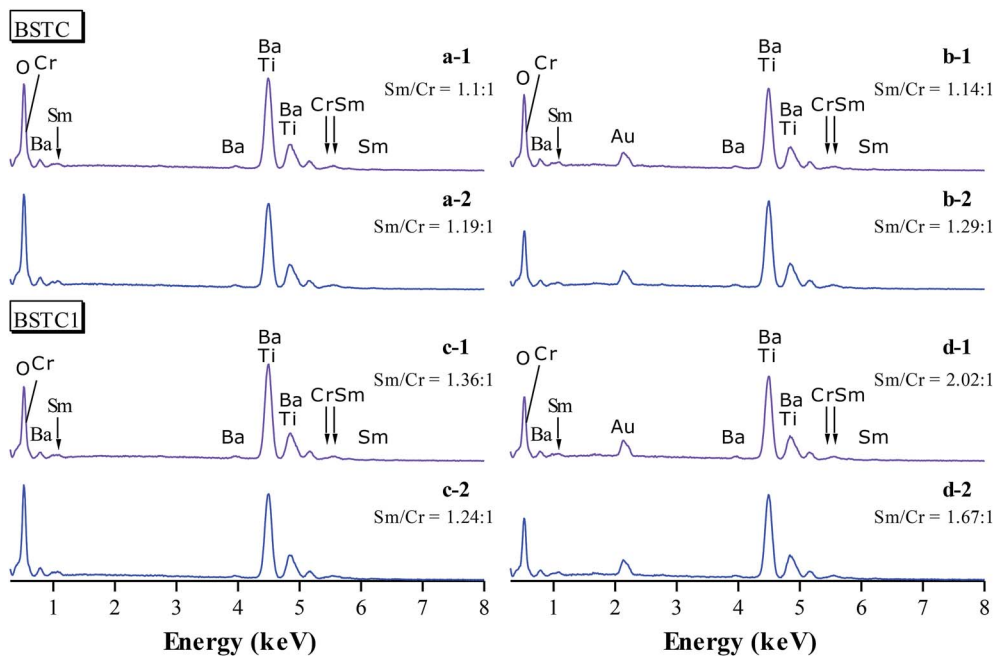
Fig. 4 EDXS at a grain of (a-1) the surface and (b-1) the interior for BSTC ceramics with $x = 0.05$, (c-1) the surface and (d-1) the interior for BSTC1 ceramics with $x = 0.05$; EDXS at a grain boundary junction [(a-2), (b-2), (c-2) and (d-2)], respectively.

performed to detect the actual ratio of Sm to Cr (Fig. 4). The data collected for two samples are showed in Fig. 4 and Table 1. The average ratio of Sm to Cr at a grain and grain boundary junction was determined to be ~1.15 and ~1.22 in the surface (no thermally-etched) and the interior (the polished and thermally-etched) for BSTC ceramics, whereas ~1.3 and ~1.85 for BSTC1 ceramics, respectively. These EDXS results reveal that (1) the concentration distribution of Sm and Cr in BSTC and BSTC1 was inhomogeneous; (2) the compositions determined from EDXS along with the expected compositions. The real Cr concentration in BSTC and BSTC1 was lower than those in formulas, *i.e.*, the concentration of Sm was higher than that of Cr and the $(Ba_{1-x}Sm_x)(Ti_{1-x}Cr_x)O_3$ and $(Ba_{1-x}Sm_x)(Ti_{1-(x-0.01)}Cr_{x-0.01})O_3$ are not the real formula of BSTC and BSTC1.

3.3. Raman scattering and photoluminescence associated with Sm^{3+} ions

In order to obtain further information on the structure and phase composition with the incorporation of Sm and Cr ions

into $BaTiO_3$ lattice, Raman spectra measurements were performed on all samples.

BSTC and BSTC1 exhibited the three common Raman bands of the cubic $BaTiO_3$, with peaks at 248 $[A_1(TO_2)]$, 520 $[A_1(TO_3)]$, and 720 cm^{-1} $[A_1(LO_3) + E(LO_3)]$.[34] The sharp band at 305 cm^{-1} (Fig. 5) $[B_1 + E(TO + LO)]$ is considered as the signature of the tetragonal phase at room temperature, and the intensity gradually weakens with increasing x, indicating a decrease in tetragonality, which corresponds with XRD results (Fig. 2 inset). In addition, although the XRD technique is a relatively rough method to determine the impurity phases, supposing that no impurity phases is present because the XRD, SEM, BSE and Raman scattering techniques did not detect any impurity phases.

The Raman charge effect at ~840 cm^{-1} (Fig. 5)[8,23,35] is the Raman evidence for aliovalent substitution in $BaTiO_3$. The band at ≥1000 cm^{-1} (Fig. 6) which attributed to photoluminescence (PL) properties in Sm^{3+}-doped $BaTiO_3$ ceramics cannot be observed using 638 nm sources, which may be attributed to the inability of the 638 nm lasers to excite the Sm^{3+} ions, similar to our previous reports.[19] Moreover, the reduction in Cr concentration by 1% for BSTC1 ($x = 0.02$) compared to BSTC ($x = 0.02$) induced strong PL properties (Fig. 5).

The Raman spectra in high-wavelength in BSTC and BSTC1 with $x = 0.02$ and 0.05 are shown in Fig. 7. The $(Ba_{1-x}Sm_x)Ti_{1-x/4}O_3$ ($x = 0.05$) ceramic, $Ba(Ti_{1-x}Cr_x)O_3$ ($x = 0.05$) ceramic, pure $BaTiO_3$ ceramic and Sm_2O_3-starting materials were prepared for comparison. This was further evidence that the band at ≥1000 cm^{-1} (Fig. 6) which attributed to photoluminescence properties in Sm^{3+}-doped $BaTiO_3$ ceramics. For the Sm_2O_3-starting materials, the bands at 595 and 643 nm consisted of three and two peaks, respectively (Fig. 7), whereas the 595 and
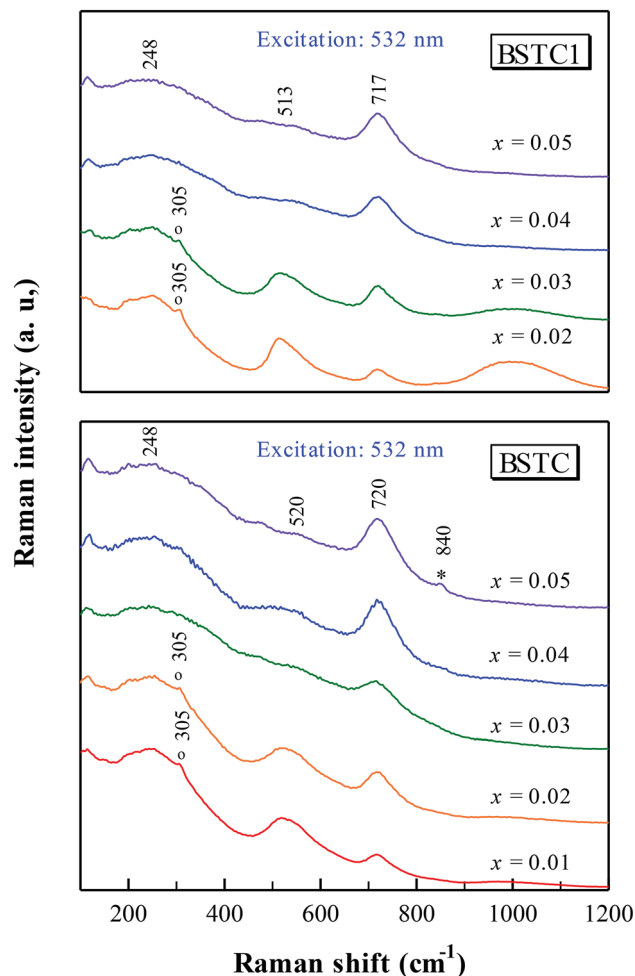
Table 1 Corresponding EDXS of molar ratio data for BSTC and BSTC1 with 0.05[a]

	Ba	Ti	Sm	Cr	O
BSTC					
a-1	16.41	18.31	0.98	0.89	63.42
b-1	17.91	18.36	0.81	0.71	62.20
BSTC1					
c-1	18.09	19.00	0.98	0.72	61.20
d-1	20.59	21.81	1.05	0.52	56.03

[a] EDXS at a grain boundary junction [(a-2), (b-2), (c-2) and (d-2)] were not occur here.

Fig. 5 Raman spectra for BSTC and BSTC1. Excitation: 532 nm laser line.
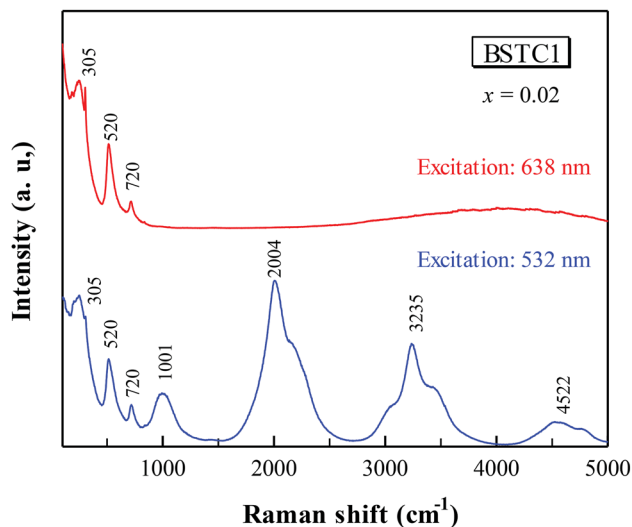

Fig. 6 Comparison of Raman spectra for BSTC1 ($x = 0.02$) upon excitation with 532 and 638 nm laser lines.

ions at Ti^{4+} sites, and B (composed of bands centered at 565, 598, and 645 nm), which is the emission of Sm^{3+} ions at Ba^{2+} sites. Murakami[16,17] have also deduced that Sm^{3+} ions occupy
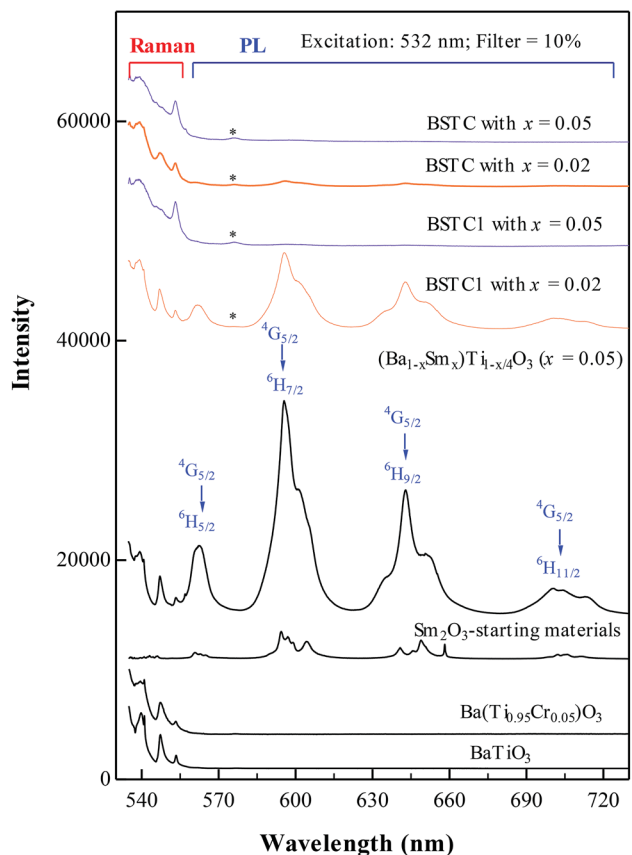
643 nm broad band of $(Ba_{1-x}Sm_x)Ti_{1-x/4}O_3$ ($x = 0.05$) ceramic showed a single-peak nature. As Cr increased, the PL intensity of Sm^{3+} ions at Ba^{2+} sites decreased sharply for BSTC and BSTC1 with $x = 0.05$ relative to S5.

The emission mechanism of PL bands in BSTC and BSTC1 is as follows: Sm^{3+} ions are excited through one-photon absorption from the ground state $^6H_{5/2}$ to the excited state $^4F_{3/2}$ that relaxes nonradiatively to the meta-level $^4G_{5/2}$ (Fig. 8). Upon 532 nm excitation, four emission peaks at approximately at 562, 595, 643 and 700 nm, corresponding to the Raman shift at 1001, 2004, 3235, and 4522 cm^{-1}, which are attributed to $^4G_{5/2} \rightarrow {}^6H_{I/2}$ ($I = 5$, 7, 9 and 11 respectively) transitions of the PL properties of Sm^{3+} in Ba^{2+} sites.[18–22] As x increased, the PL intensity of Sm^{3+} ions at Ba^{2+} sites decreased linearly and PL quenching at $x = 0.05$. The probable reason is that the formation of the defect cluster $Sm^{\bullet}_{Ba} - Cr'_{Ti}$ for a number of Sm^{3+} ions at Ba^{2+} sites and Cr^{3+} in Ti^{4+} sites for Sm and Cr co-doped $BaTiO_3$ relative to $(Ba_{1-x}Sm_x)$ $Ti_{1-x/4}O_3$ ($x = 0.05$) ceramics, which inducing energy and electron transfer.

Makishima[15] concluded that the emission spectrum of Sm^{3+} in $BaTiO_3$ is divided into parts A (composed of bands centered at 575, 585, 612, and 626 nm), which is the emission from Sm^{3+}

Fig. 7 Raman spectra in high-wavelength of Sm^{3+} in BSTC and BSTC1 with $x = 0.02$ and 0.05. Excitation: 532 nm wavelength. $(Ba_{1-x}Sm_x)Ti_{1-x/4}O_3$ ($x = 0.05$) ceramic, $Ba(Ti_{1-x}Cr_x)O_3$ ($x = 0.05$) ceramic, pure $BaTiO_3$ ceramic and Sm_2O_3-starting materials were prepared for comparison.
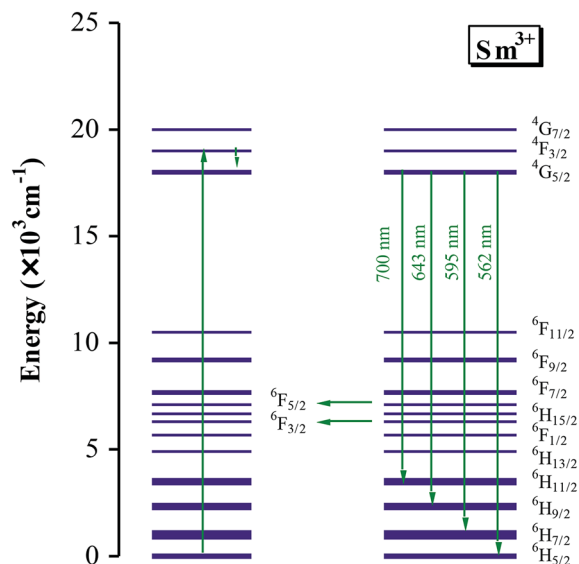
Fig. 8 Energy level diagram for Sm^{3+} ions in BSTC and BSTC1.

both Ba^{2+} and Ti^{4+} sites in specimens fired at lower temperatures and doped at higher levels and the emitting state of the A centers has a longer lifetime than that of the B centers. Hence, the weak PL band at ~575 nm associated with Sm^{3+} at Ti^{4+} sites was observed and marked with an asterisk (Fig. 7), which may be attributed that Sm^{3+} ions is substitution on Ti^{4+} sites in BSTC1 specimens.

3.4. EPR and XPS associated with valence states of Cr and Ti ions

Room temperature EPR spectra of BSTC and BSTC1 ceramics are shown in Fig. 9. A stronger signal at $g = \sim1.974$ was observed in two samples, which is associated with Cr^{3+} ($3d^3$, $S = 3/2$) ions incorporated into $BaTiO_3$. It is based on the following evidences: Ba-vacancy related $g = 1.974$ signal generally shows a very narrow linewidth.[36–38] Moreover this signal corresponds very well to measure results of Müller and Schwartz,[26,29] their Cr^{3+} causing a frequency-independent line width of 240 G. The intensity of this signal is decreased with increasing x for BSTC and BSTC1.

Temperature-dependent EPR spectra also provide more information on defects: (1) no Ti vacancies (V_{Ti}'''') signal ($g = 2.004$);[37,38] (2) no oxygen vacancies ($V_O^{\cdot\cdot}$) existed below −100 °C; (3) Ti^{3+} ($3d^1$) was also inexistent ($g = 1.932$) when $T = −183$ °C;[37,39] and (4) the EPR spectra at −183 °C (Fig. 10) did not show any signs of Cr^{5+} because of the X-band powder spectra of Cr^{5+} ($3d^1$) in $BaTiO_3$ at a low temperature of 50 K (−223 °C) was reported to evolve into three intense peaks corresponding to a g tensor over a range of 1.94 to 1.99.[40]

XPS is a powerful probe for the determination of both valence band and core levels. Fig. 11 shows the XPS spectra of Cr 2p and Ti 2p for BSTC with $x = 0.05$. The spectrum line of Cr 2p shows splitting to two peaks of Cr $2p_{3/2}$ and Cr $2p_{1/2}$, and the binding energy of $2p_{3/2}$ is 576.7, 577.8, 579.1 and 582.1 eV. Binding energy of 576.7, 577.6 and 579.1 eV was responding to
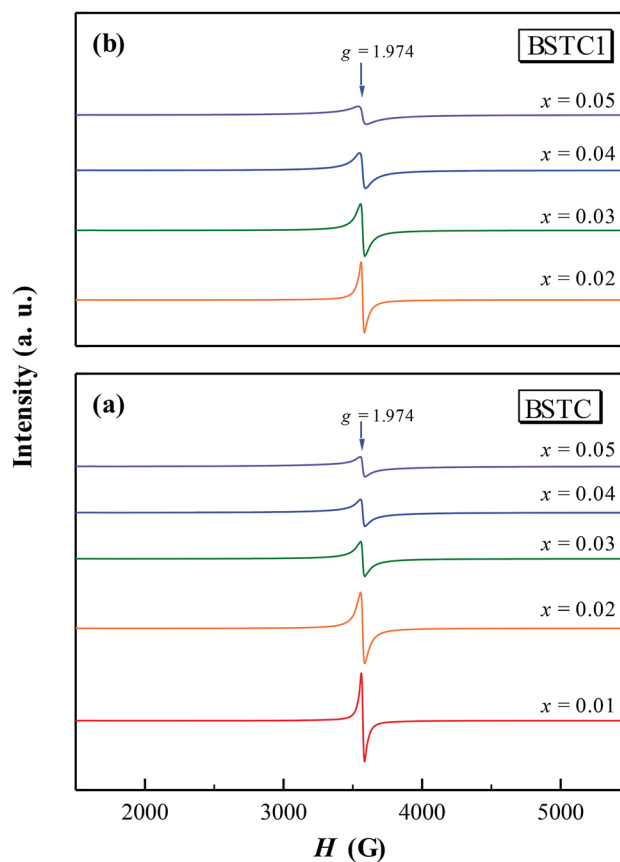

Fig. 9 Room temperature EPR spectra of (a) BSTC and (b) BSTC1.

the Cr^{3+}, Cr^{5+} and Cr^{6+}, respectively.[30,41] Two additional peaks at 582.1 eV and 591.8 eV originated from satellite peak of Cr^{3+}.[42] When the samples were prepared under air condition, due to enough oxygen existence, the Cr^{3+} ($3d^3$) can be partly oxidized to form Cr^{5+} ($3d^1$) or Cr^{6+} ($3d^0$) (Cr^{4+} ($3d^2$) is not stable and prone to be oxidized to Cr^{5+} or Cr^{6+}), three valence states of Cr can together exist in the compounds of BSTC and BSTC1. The two prominent Ti 2p peaks originated from Ti $2p_{1/2}$ at 463.8 eV and
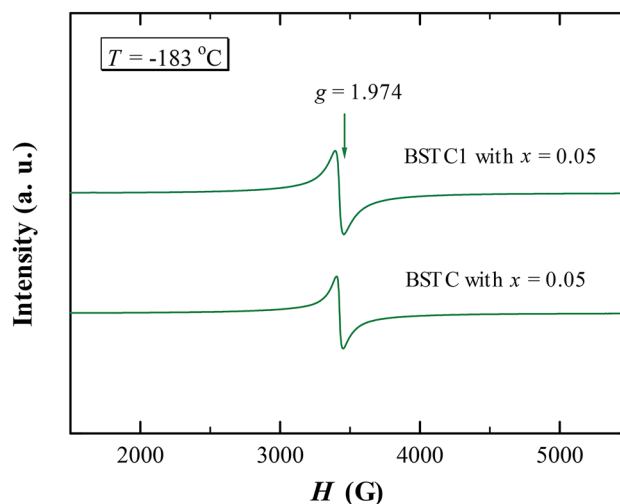

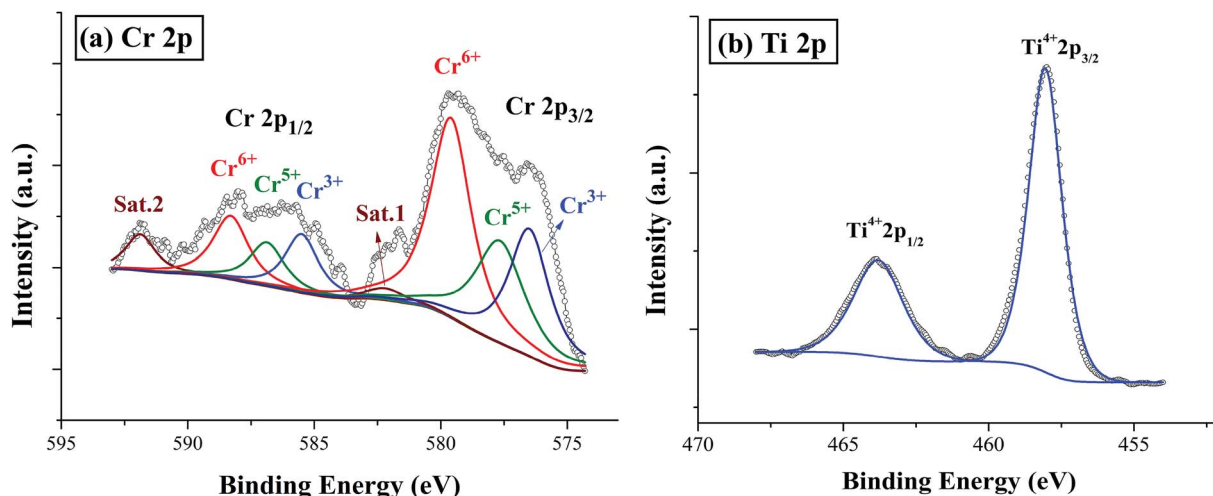**Fig. 10** Temperature-dependent EPR spectra of $x = 0.05$.

Fig. 11 XPS spectra smoothed for BSTC with $x = 0.05$: (a) Cr 2p, and (b) Ti 2p. Sat. 1 and 2 represent satellite peaks of Cr^{3+}.

Ti $2p_{3/2}$ at 457.9 eV (Fig. 11(b)), which well coincide with other researchers' work on Ti 2p XPS for $BaTiO_3$, $SrTiO_3$ (ref. 43) and $LaNaTi_2O_6$ (ref. 44) with Ti^{4+}-ion profile. This reveals that no reduction of Ti^{4+} to Ti^{3+} occurs; the Ti ions maintain the stable valence state of 4+. This fact is found to be in line with the EPR results, *i.e.*, Cr predominates as Cr^{3+} enter the Ti^{4+} sites with a stronger EPR signal (1.974), we can not detect the positional relation between molecular oxygen and titanium when acceptor like Cr^{3+} takes the Ti^{4+} sites because EPR techniques did not detect any $V_O^{\cdot\cdot}$ and Ti^{3+} ($3d^1$). The XPS spectra of BSTC1 with $x = 0.05$ were also measured and showed similar mixed valence states to those of BSTC with $x = 0.05$.

For BSTC, the concentrations of Sm and Cr are nearly equal (EDXS, Sm/Cr = ~1.15 and ~1.22) (Fig. 4) and the V_0 of BSTC is lower than that of BSTC1 (Fig. 2). Sm^{3+} ions are therefore considered to exist predominantly at the Ba^{2+} sites. In addition, some Cr ions are lost during sintering at 1400 °C, so the nominal $(Ba_{1-x}Sm_x)(Ti_{1-x}Cr_x)O_3$ is not the real formula of BSTC. It is inferred that the loss of Cr in BSTC results in the creation of Ti vacancies (cannot be detected by EPR), one can expect that high valence Cr ions will be formed to maintain the charge neutrality of the material. Thus, the established point defects are Ba^{2+} sites Sm^{3+} ($Sm_{Ba}^{\cdot}$), Ti^{4+} sites Cr^{3+} (Cr_{Ti}'), Cr^{5+} ($Cr_{Ti}^{\cdot}$) or Cr^{6+} ($Cr_{Ti}^{\cdot\cdot}$). Defect notation proposed by Kröger and Vink was adopted. The formation of $Sm_{Ba}^{\cdot} - Cr_{Ti}'$ defect complexes is predominant, which play a role in removal of V_{Ba}'' caused by Cr^{3+}.

$$Sm_2O_3 + Cr_2O_3 \rightarrow 2Sm_{Ba}^{\cdot} + 2Cr_{Ti}' + 6O_O.$$
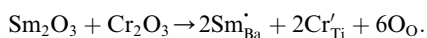
For BSTC1, most Sm^{3+} ions are located on the Ba^{2+} sites and a small number of Sm^{3+} ions at Ti^{4+} sites, which induced the formation of a self-compensation mode of $Sm_{Ba}^{\cdot} - Sm_{Ti}'$ to reduce lattice distortion and maintain the charge neutrality of the material, based on the following three points: (1) the V_0–x curve of BSTC is lower than that of BSTC1 (Fig. 2), implying that the partial occupations of Ti^{4+} sites by Sm^{3+} induce more significant expansion; and (2) unlike BSTC, BSTC1 exhibits a regular DPT behavior with a higher ε_m' and greatly lower the

dielectric loss in the ε'–T curve (Fig. 12) because of Sm^{3+} as amphoteric dopant in $BaTiO_3$ ceramics; and (3) based on the PL properties of Sm^{3+}, the weak PL band at ~575 nm (Fig. 7) associated with Sm^{3+} at Ti^{4+} sites was observed in BSTC1. The established point defects are Ba^{2+} sites Sm^{3+} ($Sm_{Ba}^{\cdot}$), Ti^{4+} sites Sm^{3+} (Sm_{Ti}'), Cr^{3+} (Cr_{Ti}'), Cr^{5+} ($Cr_{Ti}^{\cdot}$) or Cr^{6+} ($Cr_{Ti}^{\cdot\cdot}$).

3.5. Dielectric properties

All BSTC and BSTC1 ceramics are electrical insulators at room temperature. Fig. 12 shows the temperature dependence of dielectric properties of BSTC and BSTC1 ceramics measured at 1 kHz over the temperature range from −75 °C to 200 °C. The corresponding dielectric data are given in Table 2. The dielectric-peak temperature (T_m) decreased linearly at a rate of −26.3 and −24.3 °C/at% (Sm/Cr) for BSTC and BSTC1, respectively (Fig. 12 inset), which is consistent with the continuous incorporation of Sm/Cr into the $BaTiO_3$ lattice. The reason based on the following two evidences: (1) the substitution of Ba^{2+} ions by Sm ions, resulting in Ba^{2+} sites deficiency to maintain charge neutrality; and (2) the internal compressive stress increases as grain size reduces.[3,45] In addition, internal stresses were induced in grains, leading to a broadening of phase transition in BSTC with the increase of x.[3] The dielectric constant (ε') of BSTC and BSTC1 ceramics at low doping levels were higher than $BaTiO_3$ ceramics, which was also related to the dominant effect of the fine-grained on dielectric properties.[46]

For BSTC, two different peaks are observed for different compositions in BSTC with $x = 0.01$ and 0.02. The first peak on the side of higher temperatures is approximately 106 and 77.7 °C, and the second peak is located at 4 °C. The dielectric peak becomes broaden and the maximum permittivity (ε_m') gradually decreases with x, and it decreases from 7612 at $x = 0.01$ to 3020 at $x = 0.05$. The dielectric loss (tan $\delta < 0.03$) for BSTC below 100 °C was lower at low doping levels of $x \leq 0.03$. However, tan δ at $x = 0.04$ and 0.05 was higher, but the reduction of the Cr concentration in BSTC1 compared to BSTC could greatly lower the dielectric loss, such as tan δ at $x = 0.05$ was lowered from 0.1 for BSTC to 0.012 for BSTC1 (Table 2), possible
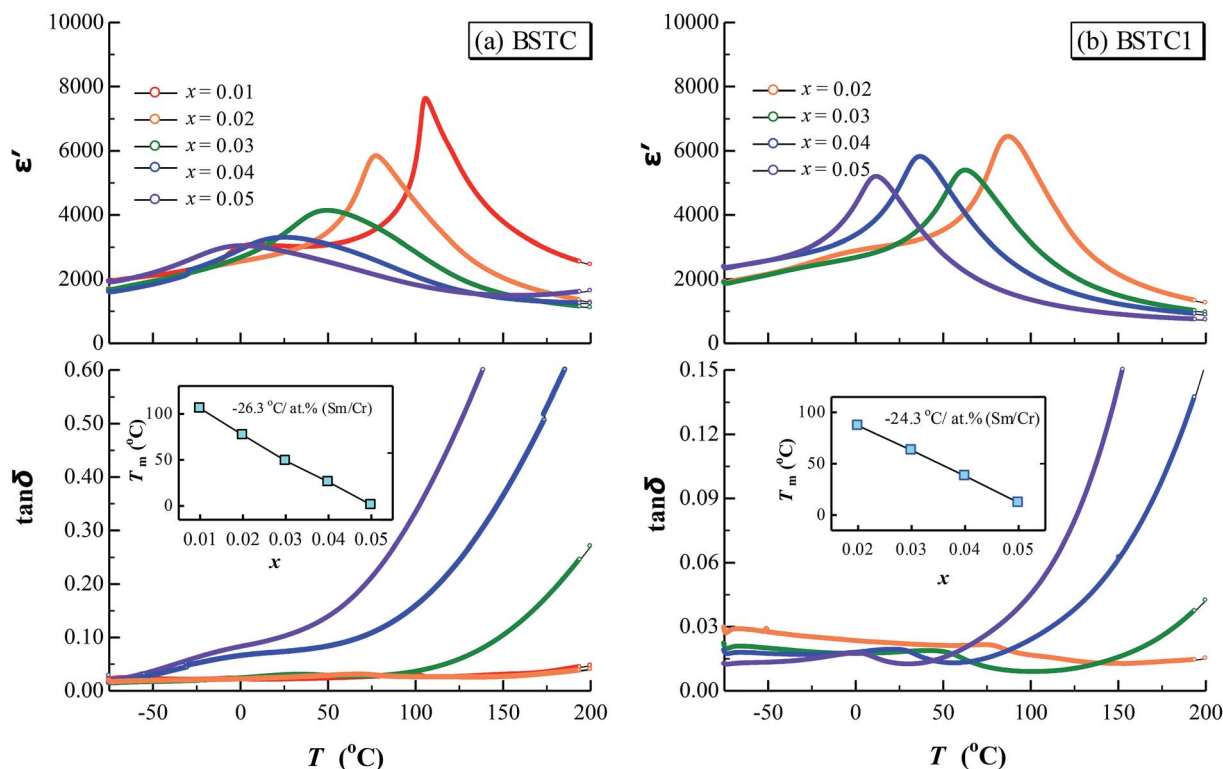
Fig. 12 Temperature dependence of the dielectric permittivity (ε') and the dielectric loss (tan δ) for (a) BSTC and (b) BSTC1. Two insets depict dielectric-peak temperature (T_m) versus the doping level (x).

Table 2 Corresponding dielectric data for BSTC and BSTC1[a]

	T_m (°C)	ε'_m	ε'_{RT}	tan δ (RT)
BSTC				
$x = 0.01$	106	7612	3009	0.02
$x = 0.02$	77.7	5817	2800	0.024
$x = 0.03$	50	4113	3367	0.028
$x = 0.04$	25.6	3271	3271	0.072
$x = 0.05$	0.8	3020	2846	0.1
BSTC1				
$x = 0.02$	87.4	6424	3068	0.022
$x = 0.03$	63	5371	3090	0.017
$x = 0.04$	37.2	5798	4808	0.019
$x = 0.05$	12.2	5174	4474	0.012

[a] ε'_m is the maximum permittivity, ε'_{RT} is the room-temperature permittivity, and tan δ is the room-temperature dielectric loss.

explanation: (1) for BSTC1, the principle of electric neutrality inhibits the electrical conductivity because of Sm^{3+} as amphoteric dopant in $BaTiO_3$ ceramics, forming a self-compensation mode of $Sm^{\cdot}_{Ba} - Sm'_{Ti}$;[47] and (2) Mn impurities play an important role in depressing electronic conduction[48] and further dielectric loss by trapping electrons in ceramic. However, the Mn^{2+} sextet signal was not observed for BSTC1, so the reduction of Mn^{4+} to Mn^{3+} is predominant[49] and the formation of $Sm^{\cdot}_{Ba} - Mn'_{Ti}$ defect complexes to prevent further reduction of Mn^{3+} to Mn^{2+}, i.e., $Mn_{Ti}^{4+} + e \rightarrow Mn_{Ti}^{3+}$.

Different from BSTC, BSTC1 exhibits a regular diffusion phase transition (DPT)[23] behavior with a higher ε' and a lower tan δ (<0.05) for $T \leq 100$ °C. The partial occupations of Ti^{4+} sites by Sm^{3+} in BSTC1 is the main reason (Fig. 10). BSTC1 with $x = 0.04$ and 0.05 show the best dielectric performance, and satisfies high-k Y5V dielectric specification with a higher $\varepsilon'_{RT} = 4474 - 4808$.

Compare to the dielectric data of BSTC and BSTC1 ceramics, when Sm content is consistent, Cr ions coexisting in Ti^{4+} sites shifts the T_m to a lower temperature, decreasing the ε' and increasing the tan δ. It is obvious that similar to La[7,14] or Ce,[12,50] Sm^{3+} (ref. 14) doping acting as a donor, predominantly dissolves in Ba^{2+} sites and effectively shifts the T_m to a lower temperature, increasing the ε' and decreasing the tan δ. This is supported by results of Dwivedi and Subramanian,[7,14] the lowering of T_m with Sm substitution is first due to its smaller size as compared to Ba which makes tetragonal phase unstable and secondly due to the bond covalency for Sm–O which will decrease shift of Ti and hence reduce its T_m. Presence of Cr on Ti^{4+} sites will lead to disrupting of Ti–O–Ti links responsible for ferroelectricity,[7] which will also lead to lowering of T_m with increasing x.

4. Conclusions

$(Ba_{1-x}Sm_x)(Ti_{1-x}Cr_x)O_3$ (x = 0.01–0.05) (BSTC) and $(Ba_{1-x}Sm_x)(Ti_{1-(x-0.01)}Cr_{x-0.01})O_3$ (x = 0.02–0.05) (BSTC1) ceramics were prepared using a traditional solid state based method. BSTC and BSTC1 with a single-phase perovskite

structure are tetragonal for $x \leq 0.03$ and pseudo-cubic for $x \geq 0.04$. Sm and Cr co-doped $BaTiO_3$ can greatly inhibit the grain growth and form a fine-grained (0.7 μm) but an inhomogeneous dopant concentration distribution (EDXS). Four emission peaks attributed to $^4G_{5/2} \rightarrow {}^6H_I$ ($I = 5, 7, 9$ and 11 respectively) indicates the transitions of Sm^{3+} at Ba^{2+} sites and the weak RS band at ~575 nm associated with Sm^{3+} at Ti^{4+} sites for BSTC1. Sm ions exists predominantly as Sm^{3+} on the Ba^{2+} sites and a small number of Sm^{3+} ions enter the Ti^{4+} sites for BSTC1; no Ti^{3+}, V_{Ti}'''', and $V_O^{\cdot\cdot}$ exists; Cr predominates as Cr^{3+} enter the Ti^{4+} sites with a stronger signal 1.974 and three valence states of $Cr^{3+}/Cr^{5+}/Cr^{6+}$ can together exist. The formation of $Sm_{Ba}^{\cdot} - Cr_{Ti}'$ defect complexes play leading roles in removal of $V_O^{\cdot\cdot}$ caused by Cr^{3+}, prevent the grain growth, and PL quenching. The dielectric-peak temperature (T_m) decreased linearly, a broadening of phase transition, and the higher ε' of BSTC and BSTC1, which were related to the dominant effect of the fine-grained. BSTC1 ceramics with amphoteric Sm^{3+} ions existed a regular DPT behavior, a rapid T_m-shifting rate of -24.3 °C/at% (Sm/Cr), a higher ε'_{RT}, a lower tan δ. BSTC1 ceramics with $x = 0.04$ and 0.05 met the Y5V specification.

Conflicts of interest

There are no conflicts to declare.

Acknowledgements

Notes and references

1 M. Budimir, D. Damjanovic and N. Setter, *Appl. Phys. Lett.*, 2006, **88**, 082903.
2 Y. Wang, K. Miao, W. Wang and Y. Qin, *J. Eur. Ceram. Soc.*, 2017, **37**, 2385–2390.
3 W. H. Lee and C. Y. Su, *J. Am. Ceram. Soc.*, 2007, **90**, 3345–3348.
4 R. Böttcher, H. T. Langhammer and T. Müller, *J. Phys.: Condens. Matter*, 2009, **21**, 075904.
5 Q. Liu, J. Liu, D. Y. Lu, W. Zheng and Ch. Hu, *J. Alloys Compd.*, 2018, **760**, 31–41.
6 F. Batllo, E. Duverger, J. C. Jules, J. C. Niepce, B. Jannot and M. Maglione, *Ferroelectrics*, 1990, **109**(1), 113–118.
7 R. K. Dwivedi, O. Parkash, D. Kumar, K. K. Srivastava and P. Singh, *J. Mater. Sci.*, 2007, **42**, 72–79.
8 D. D. Han, D. Y. Lu and X. Y. Sun, *J. Alloys Compd.*, 2013, **576**, 24–29.
9 F. Bahri, H. Khemakhem, M. Gargouri, A. Simon, R. Von der Mühll and J. Ravez, *Solid State Sci.*, 2003, **5**, 1229–1234.
10 M. T. Benlahrache, N. Benhamla and S. Achour, *J. Eur. Ceram. Soc.*, 2004, **24**, 1493–1496.
11 Y. Li, H. Cheng, M. Liu, Y. Zhang, P. Yan, C. Wang and J. Ouyang, *J. Eur. Ceram. Soc.*, 2017, **37**, 1421–1427.
12 A. Feteira and D. C. Sinclair, *J. Mater. Chem.*, 2009, **19**, 356–359.
13 D. Yu, A. m. Jin, Q. l. Zhang, H. Yang, L. Hu and D. Cheng, *Powder Technol.*, 2015, **283**, 433–439.
14 D. Li and M. A. Subramanian, *Solid State Sci.*, 2000, **2**, 507–512.
15 S. Makishima, K. Hasegawa and S. Shionoya, *J. Phys. Chem. Solids*, 1962, **23**, 749–757.
16 T. Murakami, M. Nakahara, T. Miyashita and S. Ueda, *J. Am. Ceram. Soc.*, 1973, **56**, 291–293.
17 T. Murakami, T. Miyashita, M. Nakahara and E. Sekine, *J. Am. Ceram. Soc.*, 1973, **56**, 294–297.
18 L. Zhang, H. Pan, H. Liu, B. Zhang, L. Jin, M. Zhu and W. Yang, *J. Alloys Compd.*, 2015, **643**, 247–252.
19 D. D. Han, Q. L. Liu, Y. D. Wang, C. H. Wang and D. Y. Lu, *Ceram. Int.*, 2016, **42**, 8815–8821.
20 D. Zhou, X. Cheng, Q. Fu, S. Gong and D. Zhao, *Ceram. Int.*, 2012, **38**, 6389–6397.
21 G. A. Kumar, *J. Phys. Chem. Solids*, 2001, **62**, 1327–1330.
22 Q. Zhang, Y. Zhang, H. Sun, Q. Sun, X. Wang, X. Hao and S. An, *J. Eur. Ceram. Soc.*, 2017, **37**, 955–966.
23 D. Makovec and D. Kolar, *J. Am. Ceram. Soc.*, 1997, **80**, 45–52.
24 D. Y. Lu and S. Z. Cui, *J. Eur. Ceram. Soc.*, 2014, **34**, 2217–2227.
25 Y. Pu, D. Liu and X. Shi, *Vacuum*, 2014, **99**, 38–41.
26 R. N. Schwartz and B. A. Wechsler, *Phys. Rev. B: Condens. Matter Mater. Phys.*, 1993, **48**, 7057–7069.
27 M. S. Castro, W. Salgueiro and A. Somoza, *J. Phys. Chem. Solids*, 2007, **68**, 1315–1323.
28 R. D. Shannon, *Acta Crystallogr., Sect. A: Cryst. Phys., Diffr., Theor. Gen. Crystallogr.*, 1976, **32**, 751–767.
29 H. T. Langhammer, T. Müller, R. Böttcher and H. P. Abicht, *J. Phys.: Condens. Matter*, 2008, **20**, 085206.
30 H. Qi, Y. Luan, S. Che, L. Zuo, X. Zhao and C. Hou, *Inorg. Chem. Commun.*, 2016, **66**, 33–35.
31 A. Yamaji, Y. Enomoto, K. Kinoshita and T. Murakami, *J. Am. Ceram. Soc.*, 1997, **60**, 97–101.
32 S. K. Jo, J. S. Park and Y. H. Han, *J. Alloys Compd.*, 2010, **501**, 259–264.
33 X. Liu, W. Su and Z. Lu, *J. Phys. Chem. Solids*, 2001, **62**, 1919–1921.
34 M. DiDomenico, S. H. Wemple, S. P. S. Porto and R. P. Bauman, *Phys. Rev.*, 1968, **174**, 522–530.
35 M. Kchikech and M. Maglione, *J. Phys.: Condens. Matter*, 1994, **6**, 10159.
36 D. Y. Lu and Y. Liang, *Ceram. Int.*, 2018, **44**, 14717–14727.
37 T. Kolodiazhnyi and A. Petric, *J. Phys. Chem. Solids*, 2003, **64**, 953–960.
38 T. D. Dunbar, W. L. Warren, B. A. Tuttle, C. A. Randall and Y. Tsur, *J. Phys. Chem. B*, 2004, **108**, 908–917.
39 D. Y. Lu, L. F. Yuan, W. N. Liang and Z. B. Zhu, *Jpn. J. Appl. Phys.*, 2016, **55**, 011501.
40 R. Böttcher, H. T. Langhammer and T. Müller, *J. Phys.: Condens. Matter*, 2009, **21**, 435901.
41 X. Liu, W. Su, Z. Lu, J. Liu, L. Pei, W. Liu and L. He, *J. Alloys Compd.*, 2000, **305**, 21–23.
42 A. Galtayries, R. Warocquier-Clérout, M. D. Nagel and P. Marcus, *Surf. Interface Anal.*, 2006, **38**, 186–190.

43 M. Oku, K. Wagatsuma and S. Kohiki, *Phys. Chem. Chem. Phys.*, 1999, **1**, 5327–5331.

44 J. P. Miao, L. P. Li, H. J. Liu, D. P. Xu, Z. Lu, Y. B. Song, W. H. Su and Y. G. Zheng, *Mater. Lett.*, 2000, **42**, 1–6.

45 T. Badapanda, S. K. Rout, S. Panigrahi and T. P. Sinha, *Curr. Appl. Phys.*, 2009, **9**, 727–731.

46 S. Sharma, R. K. Patel, C. Prakash and P. Kumar, *Mater. Chem. Phys.*, 2011, **130**, 191–195.

47 J. E. Sunstrom IV and S. M. Kauzlarich, *Chem. Mater.*, 1993, **5**, 1539–1544.

48 T. R. N. Kutty, P. Murugaraj and N. S. Gajbhiye, *Mater. Res. Bull.*, 1985, **20**, 565–574.

49 F. Ren and S. Ishida, *J. Ceram. Soc. Jpn.*, 1995, **103**, 759–766.

50 D. F. K. Hennings, B. Schreinemacher and H. Schreinemacher, *J. Eur. Ceram. Soc.*, 1994, **13**, 81–88.